New viscous and dissolution fingering instabilities in porous media with dead-end pores in miscible displacements

Qingwang Yuan[1], Zhiwei Ma[2], Jinjie Wang[3], Xiang Zhou[4]

[1]Bob L. Herd Department of Petroleum Engineering, Texas Tech University, Lubbock, Texas, USA
[2]Engergy Resources Engineering, Stanford University, Stanford, California, USA
[3]Faculty of Earth Resources, China University of Geosciences, Wuhan, China
[4]State Key Laboratory of Oil and Gas Reservoir Geology and Exploitation, Southwest Petroleum University, Chengdu, Sichuan, China

Key Points:

- A new dissolution fingering mechanism is reported for the first time in dead-end pore network in porous media during miscible displacements
- The interactions of viscous fingering and dissolution fingering and their influences on cleanup of NAPLs are characterized
- Six flow regimes, four of which are new, are identified in the full 'life cycle' displacements in porous media with dead-end pores

Corresponding author: Qingwang Yuan, `qingwang.yuan@ttu.edu`

Abstract

Improving the understanding of mechanisms involved in low miscible displacement efficiency is significant for a wide spectrum of applications in subsurface, from environment such as groundwater remediation and CO_2 sequestration to energy extraction such as enhanced oil recovery and geothermal recovery. Two key limiting factors to the efficiency are viscous fingering (VF) instability and dead-end pores in porous media. Previous research on VF simply assumes all pores are well connected and fluids can be mobilized by convection. However, fluids trapped in dead-end pores, such as non-aqueous phase liquids (NAPLs) in groundwater remediation, are inaccessible to convection, resulting in even less efficient displacements. Instead of the classic convection-diffusion/dispersion equation, in this work, we use a fundamentally different capacitance model to incorporate the mass transfer between two pore types in miscible displacements. The hybrid pseudo-spectral and high-order finite difference methods are employed to solve the governing equations in a fixed reference frame for simulating the flow dynamics. A new dissolution fingering (DF) mechanism is identified for the first time in miscible displacements. It is induced by VF and caused by slow dissolution of trapped NAPLs from dead-end pores to their adjacent well-connected pores. It is found the two fingering mechanisms interact and together determine the remaining NAPLs in the full 'life cycle' displacements. A simple model is also developed to accurately predict the NAPL concentration behind the finger trailing front which has not been examined previously. Six flow regimes, four of which are new, are then identified.

1 Introduction

Miscible displacement processes in porous media, where the interfacial tension between two fluids is zero, are of particular interest in a wide spectrum of applications such as soil and water contaminate remediation (Ali et al., 1995), CO_2 sequestration (Riaz et al., 2006; Gooya et al., 2019), enhanced oil recovery (Orr & Taber, 1984), geothermal recovery (Vasilyeva et al., 2006), drug delivery (Escala et al., 2019), and chromatographic separation (Mayfield et al., 2005). However, one of the major challenges is that miscible displacements usually suffer from low displacement efficiency, which results from two broad reasons (Lake, 1989): (1) *macroscopically*, the displacing fluids with less viscosity tend to bypass the displaced fluids with high viscosity, resulting in the viscous fingering (VF) instability; and (2) *microscopically*, the displaced fluids that are trapped in stagnant pockets or dead-end pores in *swept* area in porous media cannot be directly flooded by the injected fluids. Instead, the fluid flows in adjacent well-connected pores induce an eddy inside the dead-end pores and a separatrix between the two types of pores, which prevent the trapped fluids in dead-end pores from being cleaned up (Kahler & Kabala, 2016). The only mass transfer mechanism between them is molecular diffusion or dissolution under concentration gradients (Imhoff & Miller, 1996), which is extremely slow. A schematic of remediation for non-aqueous phase liquids (NAPLs) using miscible displacements is shown in Fig. 1. Understanding and characterizing the fingering instability and mass transfer of trapped fluids from dead-end pores to well-connected pores are important for groundwater remediation as well as other applications in porous media with non-negligible dead-end pores.

On one hand, the classic VF instability in miscible displacements has been extensively investigated in a large number of literature. Tan and Homsy (1988) first developed the reliable model to simulate the nonlinear VF dynamics. The authors *implicitly* assume that all pores in porous media are well connected, thus all fluids can be mobilized. The traditional convection-diffusion/dispersion equation can well characterize such displacement process. Since then, researchers used similar assumption for VF instability in a variety of scenarios for dispersion (Zimmerman & Homsy, 1991), heat transfer (Islam & Azaiez, 2010), mixing (Jha et al., 2011), inertia (Yuan & Azaiez, 2015), gravity effects (Shahraeeni et al., 2015), melting (Sajjadi & Azaiez, 2016), adsorption (Mishra et al., 2007; Rana et al., 2019), reaction (De Wit, 2020), or deposition (Sabet et al., 2020) in

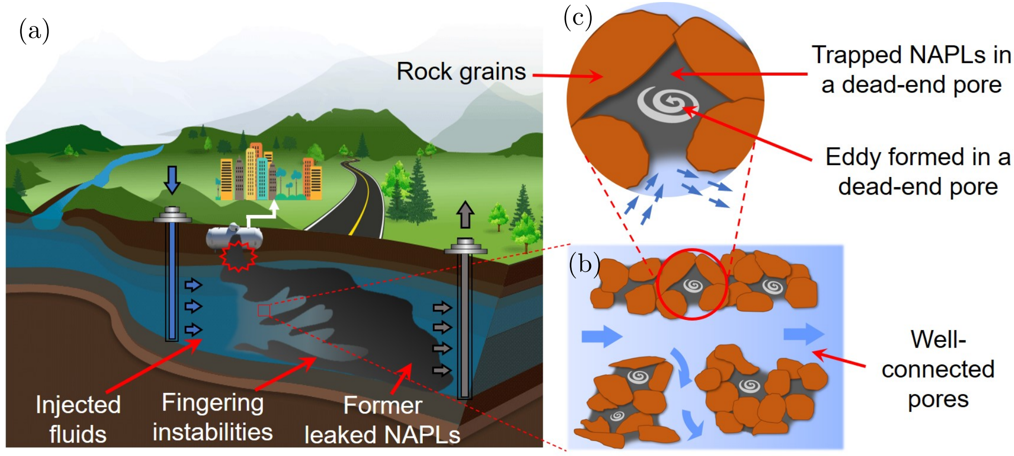

Figure 1: Schematic of fingering instabilities and the cleanup of NAPLs in groundwater remediation. (a) The VF instability is observed when the less viscous fluids miscibly displace more viscous NAPLs that are formerly leaked. (b) The NAPLs in well-connected pores (also called main channels) are easily cleaned up, but those in dead-end pores are still trapped. (c) A dead-end pore in which an eddy is formed. The trapped NAPLs in the dead-end pore is inaccessible to injected fluids through convection. These trapped fluids are sometimes called immobile fluids. But in fact, they can flow to adjacent well-connected pores through diffusion/dissolution under concentration gradient, causing rebound of NAPL concentration level after remediation. Background figure courtesy of EnviroSouth, Inc.

a simple Hele-Shaw cell (Sharma et al., 2020), heterogeneous (Tchelepi & Orr, 1994), or structured porous media (Al-Housseiny et al., 2012; Rabbani et al., 2018). In these studies, the concentration of injected fluids is nearly 100% *behind* the VF trailing front in *swept* area, i.e., no displaced fluid is left in this region. This may be reasonable for porous media in which all pores are well connected. But it is unrealistic if there are non-negligible dead-end pores distributed in porous media in which NAPLs are trapped. Such fluids cannot be directly flushed thus inaccessible to convection, but they tend to slowly diffuse or dissolve to the fluids in their adjacent well-connected pores. Consequently, the concentration of NAPLs is not zero behind the finger trailing fronts. Such mechanisms disobey the traditional convection-diffusion/dispersion equation. A fundamentally different model that could incorporate dead-end pore effects should be used. Moreover, most of previous researches focused on fingering dynamics *till* breakthrough of injected fluids in a *moving* reference frame. The benefit is that the highly accurate pseudo-spectral methods can be easily implemented because of the assumption of periodicity in all boundaries (Tan & Homsy, 1988; Zimmerman & Homsy, 1991; Jha et al., 2011). However, these methods become invalid when breakthrough happens. Seldom recent studies extended to the flows after breakthrough in a fixed reference frame (Nijjer et al., 2018; Sabet et al., 2020). When the trapped fluids in dead-end pores are incorporated in displacements, the *fixed* reference frame should be used to avoid confusions when interpreting the results. In addition, the fingering dynamics and variations of NAPLs *after* breakthrough are equally important with the those before breakthrough, as these remaining, trapped NAPLs are the main challenge in groundwater remediation and the major reason for the rebound of contaminate levels to above the regulatory limit after remediation stops (Kahler & Kabala, 2016).

On the other hand, researches on dead-end pores in rocks can date back to 1950s (Turner, 1959). It was found that the dead-end pores and trapped fluids in them are the main reasons for the tailing phenomenon observed in a 1D stable core flooding experiment in Enhanced Oil Recovery (EOR) (Lake, 1989). While in groundwater remediation, they are the key limiting factors for improving the contaminate cleanup efficiency (Kahler & Kabala, 2016). To capture the effects of dead-end pores in miscible displacements, Coats and Smith (1964) proposed the capacitance model. It can match the concentration of effluent fluids much better than the traditional convection-diffusion/dispersion equation. Using Coats and Smith (1964)'s model, Bretz et al. (1986) and Bretz and Orr (1987) indicate that the fraction of dead-end pores in porous media can be up to 34%, 42%, 51% for certain Berea sandstone, Rock Creek sandstone, and San Andres carbonate rocks, respectively. Later, similar models were developed (van Genuchten & Wierenga, 1976; Salter & Mohanty, 1982; Piquemal, 1993; Bai et al., 1995; Karadimitriou et al., 2016; Babaei & Islam, 2020). Moreover, a series of microfluidics and core flooding experiments as well as numerical modeling were conducted to examine the mass transfer between dead-end pores and well-connected pores (Wever et al., 2013; Shin et al., 2016; Kar et al., 2015; Lifton, 2016; Kahler & Kabala, 2016; Karadimitriou et al., 2016). However, these studies did not consider how the fingering instabilities under unfavorable viscosity ratio influence the local distributions of NAPLs trapped in dead-end pores in miscible displacements. There is a gap in literature on the interactions between fingering instabilities (macroscopic) and dissolution of displaced fluid from dead-end pores (microscopic). It is clear that both of them affect the overall performances of miscible displacements. Although the importance of these two aspects has been discussed by Lake (1989) in EOR and Roy et al. (1995) in the cleanup of coal tar using miscible solvent, it is however unclear how in detail they interact and determine the cleanup of NAPLs in the full 'life cycle' displacements in porous media with non-negligible dead-end pores. Note that they are not separate but coupled in displacement processes. There is also lack of fundamental understanding of the flow mechanics for miscible displacements in this specific porous medium. In this work, we will address these issues through numerical simulations. Highly accurate pseudo-spectral method and high order finite difference methods will be used to capture existing VF as well as identifying new fingering dynamics.

The present work is fundamentally different with a variety of previous studies on VF instabilities. Instead of assuming miscible displacements take place in porous media with all pores well connected, as most of researchers have done, we explicitly incorporate the fraction of dead-end pores and dissolution of trapped fluids to well-connected pores. Because of this, we will use the capacitance model proposed by Coats and Smith (1964), rather than traditional convection-diffusion/dispersion equation, for fluid flows and mass transfer in the same and different pore networks. The major novelties of this work include: (i) a new dissolution fingering (DF) mechanism is identified in porous media with dead-end pores in miscible displacements. It is induced by the preferential paths of VF and due to the slow dissolution of trapped NAPLs from dead-end pores to well-connected pores. The interaction of VF and DF instabilities is also characterized for the first time; (ii) the two fingering instabilities on the remaining NAPLs for the full 'life cycle' displacements are well characterized in both well-connected and dead-end pore networks, instead of only focusing on the displacements before breakthrough in previous studies; and (iii) six flow regimes are identified, four of which have never been reported.

2 Mathematical Models

2.1 Physical Model

We assume the miscible displacements in the cleanup of NAPLs in groundwater system take place in a 2D horizontal porous medium, as shown in Fig. 2. The porous medium is homogeneous with length L_x and width L_y. Initially, it is saturated by NAPLs with a high viscosity μ_2. The miscible fluids such as solvent with less viscosity μ_1 are injected from the left boundary to displace NAPLs at a constant, uniform injection rate U. The displaced fluids are then produced freely from the outlet. The initial interface

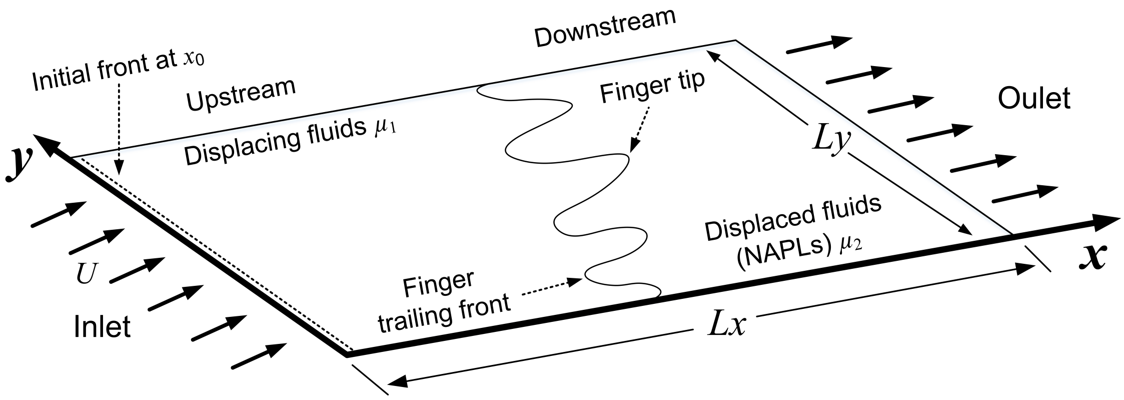

Figure 2: Schematic of miscible fingering instabilities in porous media.

of two fluids is located at x_0. To simply the problem, we further assume all fluids are incompressible, and the flows are in the laminar regime.

For the porous media with non-negligible dead-end pores, we assume the fractions of well-connected and dead-end pore networks are f and $1-f$, respectively, in any control volume in the total pore space. In other words, the distribution of dead-end pores is uniform in the whole porous media. Once the NAPLs in well-connected pores are flushed, those in dead-end pores will slowly diffuse or dissolve to the fluids in their adjacent well-connected pores. Such mass transfer depends on many factors (Jasti et al., 1988). For simplicity, here we refer it to dissolution and do not distinguish the differences between diffusion and dissolution. Note this is different with the solid dissolution discussed in Sajjadi and Azaiez (2016) for melting or Szymczak and Ladd (2009) for wormhole formation. It should also be mentioned that the adsorption of NAPLs by rock matrix is not considered here, although it has similar tailing phenomenon in effluent fluids (Mishra et al., 2007; Rana et al., 2019).

2.2 Governing Equations

The miscible displacements in porous media with non-negligible dead-end pores can be described by the following equations in the dimensional form:

$$\nabla \cdot \mathbf{u} = 0 \tag{1}$$

$$\nabla P = -\frac{\mu_m}{k}\mathbf{u} \tag{2}$$

$$f\frac{\partial C_m}{\partial t} + (1-f)\frac{\partial C_{im}}{\partial t} + \frac{\mathbf{u}}{\phi} \cdot \nabla C_m = D\nabla^2 C_m \tag{3}$$

$$\frac{\partial C_{im}}{\partial t} = \alpha(C_m - C_{im}) \tag{4}$$

where $\mathbf{u} = (u, v)$ denotes the 2D Darcy velocity vector in well-connected pore network; P pressure; μ viscosity; k permeability; C concentration; t time; ϕ total porosity, and D is a constant coefficient. Subscripts m and im represents the fluids in well-connected and dead-end pore networks, respectively. α is the first-order mass transfer rate coefficient between two pore types. For convenience, in the following, the term μ_m/k is simply written as μ_m since k is assumed to be constant in this study.

Equations (3) and (4) are called capacitance model which is first proposed by Coats and Smith (1964) to incorporate the effects of stagnant volume (i.e., the dead-end pores) in porous media. Although later there are other similar models proposed, we will not distinguish their differences and employ Coats and Smith (1964)'s model in this study. Different with the original model, we separate α and $1-f$ in Eq. (4). This does not affect the simulations or results but will allow us to analyze the effects of f and α separately in future research. Note the coefficient D can be either a *constant* diffusion or dispersion coefficient in this study. But it can be extended to the case considering concentration-dependent diffusion and/or velocity-induced, anisotropic dispersion (Yuan et al., 2017a), depending on different scenarios and applications. Previous studies indicate that the dispersion anisotropy does not affect the qualitative features of flow dynamics (Zimmerman & Homsy, 1991; Jha et al., 2011; Ghesmat & Azaiez, 2008; Sabet et al., 2020). Therefore, in this work, we use a constant D and will solve the equations in dimensionless form.

To non-dimensionalize the governing equations (1)-(4), the diffusive scaling is used (Sajjadi & Azaiez, 2013).

$$\begin{aligned} &(x^*, y^*) = \frac{(x,y)}{D\phi/U}; \quad \mathbf{u}^* = \frac{\mathbf{u}}{U/\phi}; \quad t^* = \frac{t}{\frac{D\phi^2}{U^2}}; \quad C_m^* = \frac{C_m}{C_2}; \\ &C_{im}^* = \frac{C_{im}}{C_2}; \quad \mu^* = \frac{\mu}{\mu_1}; \quad P^* = \frac{P}{\mu_1 D\phi} \end{aligned} \tag{5}$$

The star symbols represent dimensionless parameters. With the diffusive scaling and after integrating Eq. (4) into Eq. (3), the governing equations in dimensionless form are,

$$\nabla \cdot \mathbf{u}^* = 0 \tag{6}$$

$$\nabla P^* = -\mu_m^* \mathbf{u}^* \tag{7}$$

$$f\frac{\partial C_m^*}{\partial t^*} + Da(1-f)(C_m^* - C_{im}^*) + \mathbf{u}^* \cdot \nabla C_m^* = \nabla^2 C_m^* \tag{8}$$

$$\frac{\partial C_{im}^*}{\partial t^*} = Da(C_m^* - C_{im}^*) \tag{9}$$

where $Da = \alpha D\phi^2/U^2$ is the Damköhler number which is the ratio of a characteristic time for convection to a characteristic time for mass transport between two pore types (Lake, 1989). Note the definition of Da in this work is different with those in reactive flows (Almarcha et al., 2010) or wormhole formation (Szymczak & Ladd, 2009). Based on diffusive scaling, the coefficient D appears in the Péclet number $Pe = UL_x/(D\phi)$ which represents the length of the domain in dimensionless form.

Similar to the previous study (Tan & Homsy, 1988), the viscosity-concentration relation is given by

$$\mu_m^* = e^{RC_m^*} \tag{10}$$

where $R = ln(\mu_2/\mu_1)$ is the log ratio of NAPL viscosity to that of injected fluids. Equation (10) is applied to the fluids in well-connected pore network. In this work, there is no need to calculate the viscosity of fluids in dead-end pores as they are inaccessible to convection. This is also reflected by the convection term $\mathbf{u}^* \cdot \nabla C_m^*$ in Eq. (8) which is only for C_m^*. Because of this, the Darcy's law is also only used for fluids in well-connected pore network, as shown in Eq. (7).

Note all the equations in this work are given and will be solved in a *fixed* reference frame. This will bring substantial advantages and avoid confusions when analyzing fingering dynamics and variations of remaining NAPLs. On the contrary, if a Lagrangian moving reference frame is used for the present research, as what have been done by most of previous researchers (Tan & Homsy, 1988; Islam & Azaiez, 2005; Jha et al., 2011), the instantaneous swept area in dead-end pore network will move at a constant injection rate, making the results hard to understand and interpret. Another advantage is that the flows can be simulated for any long time after breakthrough using a fixed reference frame, while the moving reference frame is only valid in the flow direction before breakthrough. Since one of our focuses is to characterize the remaining NAPLs in the full 'life cycle' displacements, the fixed reference frame is the best option.

In the following, for convenience, all the asterisks are dropped.

2.3 Streamfunction-Vorticity Formulation

The velocity is not solved directly, instead, the streamfunction-vorticity formulation is used for the velocity terms, as shown in the following.

$$u = 1 + \frac{\partial \psi}{\partial y} \tag{11a}$$

$$v = -\frac{\partial \psi}{\partial x} \tag{11b}$$

$$\omega = \frac{\partial v}{\partial x} - \frac{\partial u}{\partial y} = -\nabla^2 \psi \tag{11c}$$

The advantage is that the continuity equation (6) can be automatically met. In Eq. (11a), the velocity u is expressed as the sum of a constant base state and a perturbation term $\frac{\partial \psi}{\partial y}$.

Taking curl of Darcy's law (Eq. 7) and eliminating the pressure term, we obtain

$$\omega = -R\left[\frac{\partial \psi}{\partial x}\frac{\partial C_m}{\partial x} + \left(\frac{\partial \psi}{\partial y} + 1\right)\frac{\partial C_m}{\partial y}\right] \tag{12}$$

Equation (8) then takes the form of,

$$f\frac{\partial C_m}{\partial t} + Da(1-f)(C_m - C_{im}) + \left(1 + \frac{\partial \psi}{\partial y}\right)\frac{\partial C_m}{\partial x} - \frac{\partial \psi}{\partial x}\frac{\partial C_m}{\partial y} = \nabla^2 C_m \tag{13}$$

Equations (12), (13), and (9) will be solved for C_m, C_{im}, and ψ using the numerical techniques discussed in the next section.

2.4 Numerical Techniques

To accurately and efficiently solve the governing equations while considering the actual fluid flows, we first make several assumptions on the initial and boundary conditions. We assume an initial sharp front between the injected fluids and NAPLs is located at $x_0 = 1/64$ of the domain in x direction. This does not affect the results but allows us to add random perturbations on the initial front to initiate the fingering instabilities. Both displacing fluids and NPALs are distributed uniformly in the domain at the initial time. As to boundary conditions, we assume $C_m = C_{im} = 0$ at left boundary (inlet) for all the times due to the injection of displacing fluids. For the right boundary (outlet), fluids are allowed to flow out freely. In y direction, a periodic boundary condition is employed, same with the previous researches (Tan & Homsy, 1988; Islam & Azaiez, 2005; Sabet et al., 2020).

With the above conditions, the combination of several advanced numerical techniques is used. First, a pseudo-spectral method, the Fast Harlety Transform, is used to calculate the y derivatives because of the periodicity (Islam & Azaiez, 2005). While in x direction, the sixth-order finite difference method is used for x derivatives (Lele, 1992; Sari & Gürarslan, 2009).

For time advancement, the second-order fully implicit alternating-direction implicit (ADI) method is used (Islam & Azaiez, 2005) to solve Eqs. (8) and (9). A whole time step Δt is divided into two equal half time step. In each half time step, a tridiagonal system of equations is obtained and solved using the Thomas matrix algorithm (Hoffman & Frankel, 2001). More details for the implementation of ADI method in the domain and at boundaries can be found in Appendix A. These techniques are capable of capturing the complex nonlinear fingering dynamics in the full 'life cycle' displacements for Pe up to 10,000 at $R = 3$.

To validate our self-developed codes, the following tests have been performed. First, we used two different methods for the calculations of x derivatives by (i) imposing a periodic extension of displacement front in the downstream of the domain (Tan & Homsy, 1988; Zimmerman & Homsy, 1991; Yuan et al., 2017b); and (ii) simply doubling the whole domain in the flow direction. These methods enforce periodicity in x direction so that the Fast Hartley Transform is used for calculating x derivatives. While exactly the same fingering dynamics is obtained comparing with our sixth-order finite difference method (FDM), these two methods are however incapable for our research. Specifically, the first method creates two interfaces along the flow direction in the domain. In a fixed reference frame, it is only valid before the two interfaces interact or the right interface reaches the right boundary, whenever which one happens earlier. The flows after breakthrough cannot be modeled using this method. The second method can simulate the flows for a longer time, but it also suffers the similar issues. Moreover, it needs more computational time because of the doubled domain. In contrast, our high-order FDM method can achieve the spectral accuracy, need less time, and is capable of simulating the flows for an infinite long time after breakthrough. Second, we compared our results for a stable displacement at $R = 0$ with the analytical solution given by Brigham (1974). A perfect match on the spatial and temporal variations of concentration profiles is obtained. Third, we set $f = 1$ (no dead-end pores in porous media) and compared our fingering dynamics with that in Islam and Azaiez (2005) and Yuan and Azaiez (2014). An acceptable agreement was obtained in terms of VF count, length, and width. Finally, we varied the time step Δt and grid size N_x and N_y, and results are stable in different tests. In this work, we fixed $\Delta t = 0.1$ and $N_x = N_y = 512$, which allows us to accurately capture the complex fingering dynamics while completing the simulations in an acceptable length of time.

In this work, unless mentioned otherwise, we fix the values of parameters such that the fraction of well-connected pores $f = 0.6$ (i.e., fraction of dead-end pores is $1-f = 0.4$), Damköhler number $Da = 0.001$, Péclet number $Pe = 2000$, log viscosity ratio $R = 3$, and aspect ratio of the domain $A = L_x/L_y = 2$. The values of Da and f are chosen based on measurements in core flooding experiments by Baker (1977). The Pe and R are within the ranges reported in literature (Tan & Homsy, 1988; Jha et al., 2011; Meng & Guo, 2016). Although they all have strong influences on fingering dynamics and variations of NAPLs, a parametric study will however be conducted in the future. In the following discussions, C represents the concentration for traditional case without considering dead-end pores, while C_m, C_{im}, and C_T represent those in well-connected pores, dead-end pores, and overall porous media, respectively.

3 Results and Discussion

In this section, we first examine the flow dynamics and compare with classic viscous fingering (VF) instability without considering dead-end pores. A new dissolution fingering (DF) is reported in miscible displacements. We then focus on the variations of y-averaged NAPLs and establish a simple model to accurately predict the remaining NAPLs behind the finger trailing front. At the end, we discuss six flow regimes we identified in the full 'life cycle' displacement processes.

To avoid confusions, VF means either the classic fingering without dead-end pores or that in well-connected pore network when dead-end pores are considered in porous media in this work. The DF is only for fingering in dead-end pore network, while we simply refer the fingering instabilities for the flow dynamics in the whole porous media with dead-end pores.

3.1 New Dissolution Fingering Instabilities

Figure 3 depicts the concentration profiles in porous media with and without considering the dead-end pores at time $t = 985$. Yellow and dark colors represent the injected solvent and NAPLs, respectively. At an initial time, a sharp interface between two fluids is located at the 1/64 of the domain in x direction (not shown in this plot). Later, as displacements continue, the interface becomes unstable and eventually highly distorted

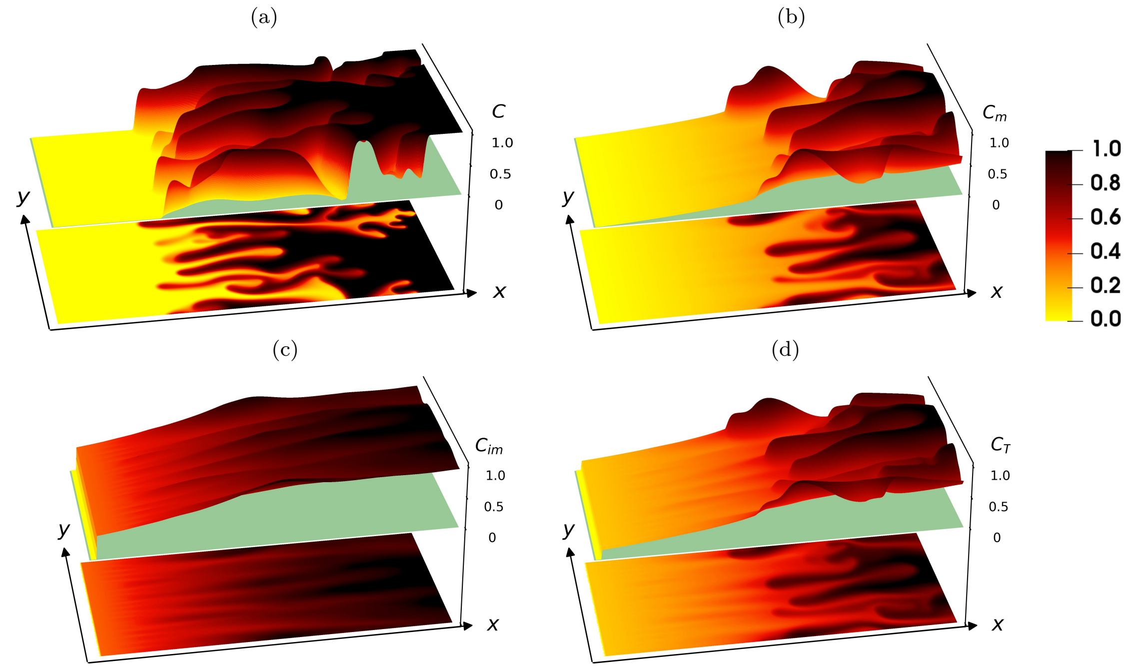

Figure 3: The 3D surface (upper) and 2D contour (lower) plots of fingering instabilities in miscible displacements at time $t = 985$, $Pe = 2000$, and $R = 3$. Yellow and dark colors represent injected solvent and NAPLs, respectively. (a) Concentration profiles C in porous media *without* dead-end pores ($f = 1.0$). (b)-(d) Concentration profiles for C_m in well-connected pore network, C_{im} in dead-end pore network, and C_T ($C_T = f \cdot C_m + (1 - f) \cdot C_{im}$) in the whole porous media with dead-end pores, respectively, at $f = 0.6$ and $Da = 0.001$.

with the finger tips reaching the right boundary, resulting in the breakthrough of injected fluids. An animation of the full 'life cycle' displacement processes can be found in Supplementary information.

Specifically, the viscous fingering (VF) structures for the case *without* considering dead-end pores in porous media in Fig. 3a are consistent with what reported previously (Tan & Homsy, 1988) on the two aspects: (1) when breakthrough happens at time $t = 985$, a large amount of NAPLs is unswept (the dark color in Fig. 3a); and (2) the concentration of NAPLs behind the VF trailing front is 0, indicating the NAPLs are *completely* cleaned up in this region. As discussed previously, this is reasonable if there is a negligible proportion of dead-end pores in porous media, thus all NAPLs are mobile and can be directly flushed in swept area. However, this model is unrealistic considering the fact that significant amount of water or solvent is needed to reduce the contaminant to regulatory limit as well as the rebound of contaminant concentration after the pump-and-treat process stops (Kahler & Kabala, 2016). The effects of dead-end pores in subsurface porous media should be incorporated.

Figures 3b-d depict the concentration profiles at $t = 985$ in porous media with 40% dead-end pores ($f = 0.6$). Although similar unstable flows are observed compared to Fig. 3a, different fingering characteristics and new instability mechanism can be identified. Specifically, the breakthrough of injected fluids happens earlier at $f = 0.6$ and $Da = 0.001$ as the convection takes place only in well-connected pore network (60% of the total porosity). However, the fingering tip splitting is much weaker. This is mainly because the trapped NAPLs dissolve to the displacing fluid and increase its viscosity, leading to the reduction of effective viscosity ratio.

Another obvious difference, compared with Fig. 3a, is that the concentration of NAPLs C_m and C_T gradually increases from 0 at the inlet, indicating the NAPLs cannot be completely cleaned up even in the well-connected pores. This is because of the slow dissolution of trapped NAPLs (C_{im}) from the dead-end pores to well-connected pores. Since the dead-end pores are inaccessible to convection, they act like a source of NAPLs. This effect will last for a long time in the displacements.

From another point of view, due to the low dissolution rate, the trapped NAPLs in dead-end pores cannot be cleaned up *immediately* when the injected fluids sweep the adjacent well-connected pores. The temporal and spatial distributions of such NAPLs (C_{im}), after displacements start, are determined by the dimensionless dissolution rate Da and the time-varying preferential flow paths of injected fluids in well-connected pore network. In other words, it is the dissolution and VF instability that induces the unstable, non-uniform distribution of NAPLs in a finger-like pattern in dead-end pore network. We therefore refer this new fingering mechanism to dissolution fingering (DF) or VF induced fingering, as shown in Fig. 3c. This is the first time that the DF is reported in *miscible* displacements. It is different from what reported by Imhoff and Miller (1996), Imhoff et al. (1996), and Zhao et al. (2011) where the DF is identified in *immiscible* displacements and induced by the change of relative permeability and non-uniform distribution of the NAPL ganglia in porous media *without* dead-end pores. Their DF structures are also much simpler. However, in both scenarios, the dissolution plays a role in forming the DF instability.

Although the DF is induced by VF, it does not exactly mimic the instantaneous VF structures. Instead, the DF is formed by the *accumulated* dissolution of NAPLs along the time-varying preferential flow paths of injected fluids in well-connected pore network. Therefore, in the corresponding region behind the VF trailing front in Figs. 3b and 3c, the C_{im} exhibits clear unstable structures, while the C_m gradually increases in a stable way in the same region. Note that the C_m and C_{im} are coupled and affect each other, resulting in different fingering instabilities and NAPL distributions in the overall porous media (C_T) in Fig. 3d, compared to those in Fig. 3a.

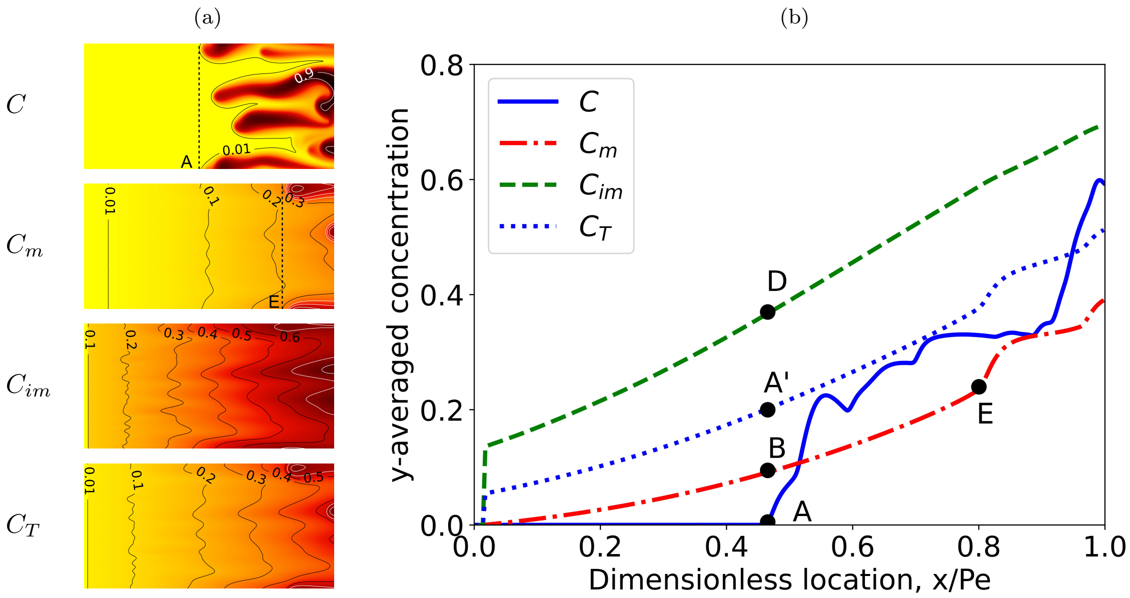

Figure 4: The comparison of concentration profiles at time t = 2000, Pe = 2000, and R = 3 with and without considering dead-end pores in porous media for C, C_m, C_{im} and C_T. (a) Concentration fields and contours. (b) y-averaged concentration profiles. x is the length of the domain and varies from 0 to Pe in dimensionless form. Point A corresponds to the trailing front of VF for C at location around 0.47 of the domain in longitudinal direction (without dead-end pores in porous media). Points A′, B, D are the y-averaged concentration for C_m, C_{im}, and C_T, respectively, at the same location. Point E corresponds to the trailing front of C_m.

3.2 NAPLs Behind the Finger Trailing Front

We also plot the concentration fields and y-averaged concentration profiles at t = 2000, as shown in Fig. 4. For convenience, we define the finger trailing front x_t/Pe as the location when the backward fingers of displaced fluids do not have obvious effects on fluid concentration. This corresponds to the line A and E for C and C_m, respectively, in Fig. 4a.

Although focusing on different aspects, most of the previous studies on fingering dynamics and their effects on sweep efficiency are limited to the displacements *till* breakthrough in porous media *without* dead-end pores (Tan & Homsy, 1988; Chen & Eckart, 1998; Islam & Azaiez, 2005; Ghesmat & Azaiez, 2008; Sajjadi & Azaiez, 2014; Norouzi & Shoghi, 2014). In their models, there is no need to study the variations of fluids (NAPLs in this case) *behind* the finger trailing fronts as the displaced fluids are completely cleaned up, meaning their concentration is 0 in this region. However, as indicated in Figs. 3 and 4, a certain concentration of NAPLs remains behind the finger trailing fronts in both well-connected and dead-end pores in this study. In this section, we first analyze the variations of NAPLs concentration by examining the concentration fields, contours, and y-averaged concentration profiles. We then develop the empirical model to predict the y-averaged concentration profiles *behind* the finger trailing front.

Several important observations can be obtained in Fig. 4. First, for the case without dead-end pores, the concentration C varies from 0.01 to 0.9 sharply ahead of the finger trailing fronts (right side of line A, $x_t/Pe \approx 0.47$ of the domain to downstream), while C is nearly 0 at upstream (left side of line A, upstream to $x_t/Pe \approx 0.47$ of the domain). This is confirmed by the y-averaged concentration profile in Fig. 4b. In comparison, if the porous media contain 40% dead-end pores ($f = 0.6$), the concentration

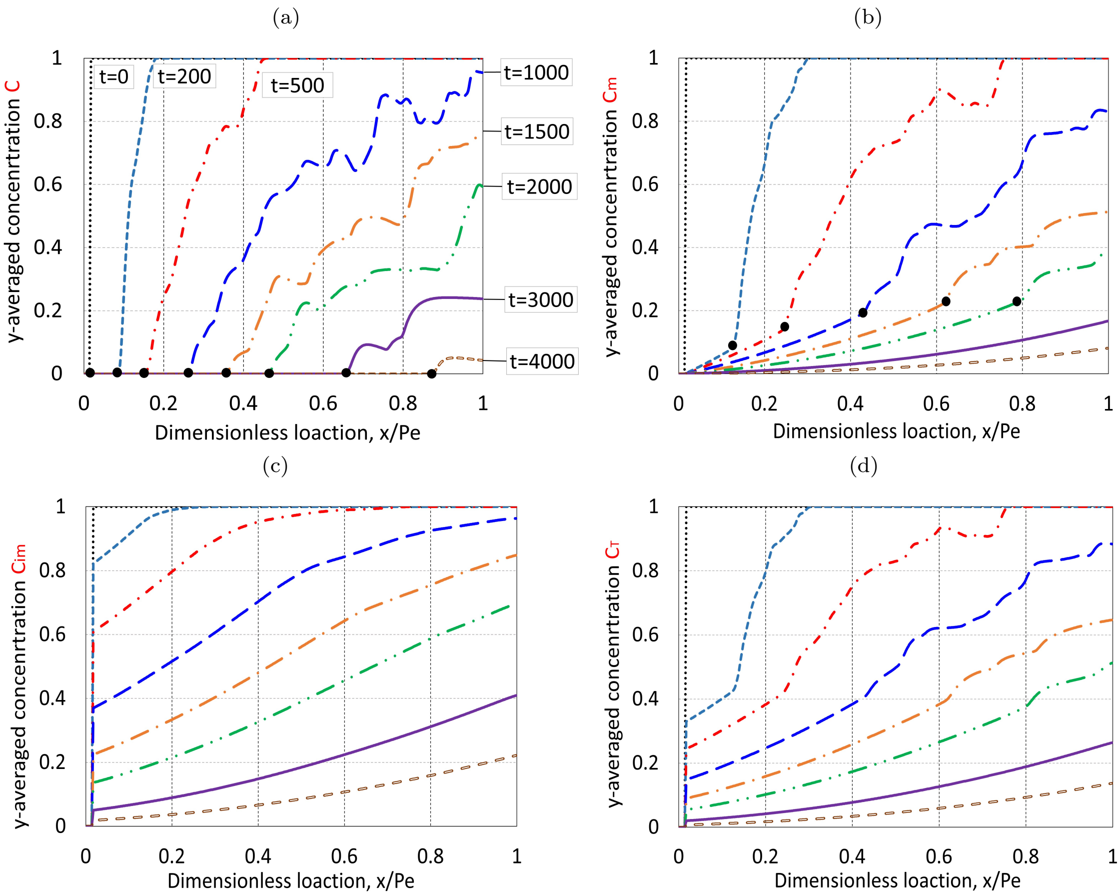

Figure 5: y-averaged NAPL concentration profiles at $Pe = 2000$ and $R = 3$ for (a) C without dead-end pore effects, (b) C_m for well-connected pore network, (c) C_{im} for dead-end pore network, and (d) C_T for the overall porous media (in plots b-d, $f = 0.6$ and $Da = 0.001$). Same curve styles are used for different concentrations at their corresponding times. Dark solid circles represent the locations of fingering trailing fronts x_t/Pe at different times.

contours and y-averaged concentration profiles for C_m, C_{im}, and C_T increase smoothly in the flow direction. Specifically, behind the finger trailing fronts (left side of line E in Fig. 4a), the NAPL concentration C_m varies from 0.01 to 0.2, while the C_{im} is much higher with $C_{im} = 0.1$ even at the inlet. Overall, the concentration of remaining NAPLs C_T in the whole domain varies from 0 to up to 0.4 behind the finger trailing front, a large difference with that of C without dead-end pores.

Note when locating finger trailing fronts x_t/Pe, the values of concentration are not exactly the same for the scenarios with and without considering dead-end pores. However, the same criterion is applied; the y-averaged concentration profiles exhibit quite different characteristics behind and ahead of the finger trailing fronts. For example, behind the finger trailing fronts in Fig. 4b, either C is 0 or C_m changes in a certain pattern (left side of points A and E). While ahead of the finger trailing fronts (right side of points A and E), both C and C_m exhibit obvious fluctuations because of the strong fingering instabilities. Note that for the case considering dead-end pores, we use the changes of C_m to determine its finger trailing front, instead of C_{im} or C_T. This is because the concentration gradient in well-connected pore network is sharper near the finger trailing front, as shown in Figs. 3 and 4.

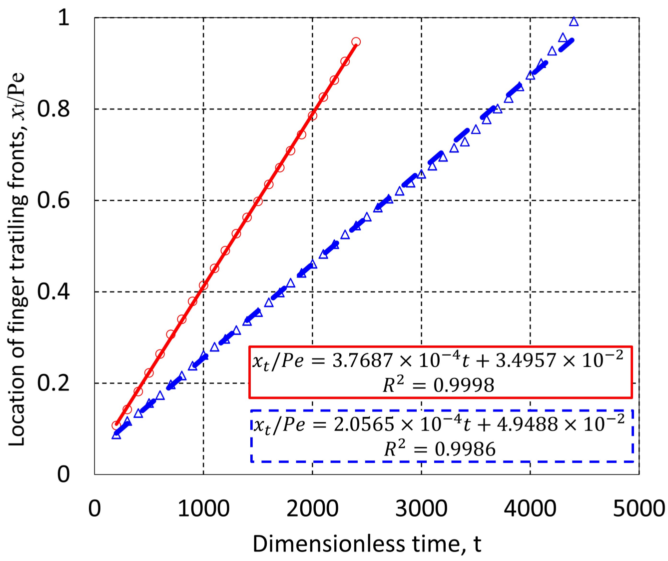

Figure 6: The variation of finger trailing fronts x_t/Pe with time at $Pe = 2000$ and $R = 3$. Blue curve and symbols are for that without dead-end pores (C). Red curve and symbols are for that with dead-end pore effects (C_m at $f = 0.6$ and $Da = 0.001$). Symbols represent the x_t/Pe obtained from the y-averaged concentration profiles using nonlinear numerical simulation. Straight lines are obtained by curve fitting.

A more complete comparison of the y-averaged concentration profiles is shown in Fig. 5. A contact zone or mixing zone can be defined when the y-averaged concentration of NAPLs starts to increase from 0 to 1 (Tan & Homsy, 1988; Jha et al., 2011). For the classic case without dead-end pores in porous media, the contact zone moves towards the downstream of the domain with time, as shown in Fig. 5a. This is consistent with the previous research (Tan & Homsy, 1988), although a moving reference frame is used there. However, when the porous media contain 40% dead-end pores, the contact zone for the overall concentration C_T always starts from the inlet as the NAPLs in dead-end pores C_{im} cannot be cleaned up completely.

Ahead the x_t/Pe (downstream), the variations of y-averaged concentration profiles for C_m, C_{im}, and C_T are too much strongly affected by fingering instabilities and can only be obtained through nonlinear numerical simulations, as shown by the fluctuations of curves in Fig. 5. While behind the finger trailing front, their variations seem to follow a certain pattern and may be accurately predicted by a simple empirical model. Note in this region, the fingering instabilities still play a role in concentration contours and y-averaged concentration profiles. Thus, an analytical solution cannot be achieved to predict their variations. Since it is for the region behind fingering trailing front, we start with the propagation rate of this front x_t/Pe.

The propagation of finger trailing fronts x_t/Pe with time is represented by the dark solid circles in Fig. 5a and 5b and plotted in Fig. 6 with symbols. x_t/Pe seems to propagate at a constant rate for both cases with and without dead-end pores in porous media, as indicated by the curve fitting. The finger trailing front for C_m propagates nearly two times faster than its counterpart C without dead-end pore effects. At a later time, the trailing front for C (blue symbols) moves slightly faster. This linear relation for C_m allows us to determine the region that our simple empirical model is valid for predicting y-averaged concentration without needing time-consuming nonlinear simulations.

Since the overall concentration C_T is determined by C_m in well-connected pore network and C_{im} in dead-end pore network (i.e., $C_T = f \cdot C_m + (1-f) \cdot C_{im}$), we first ob-

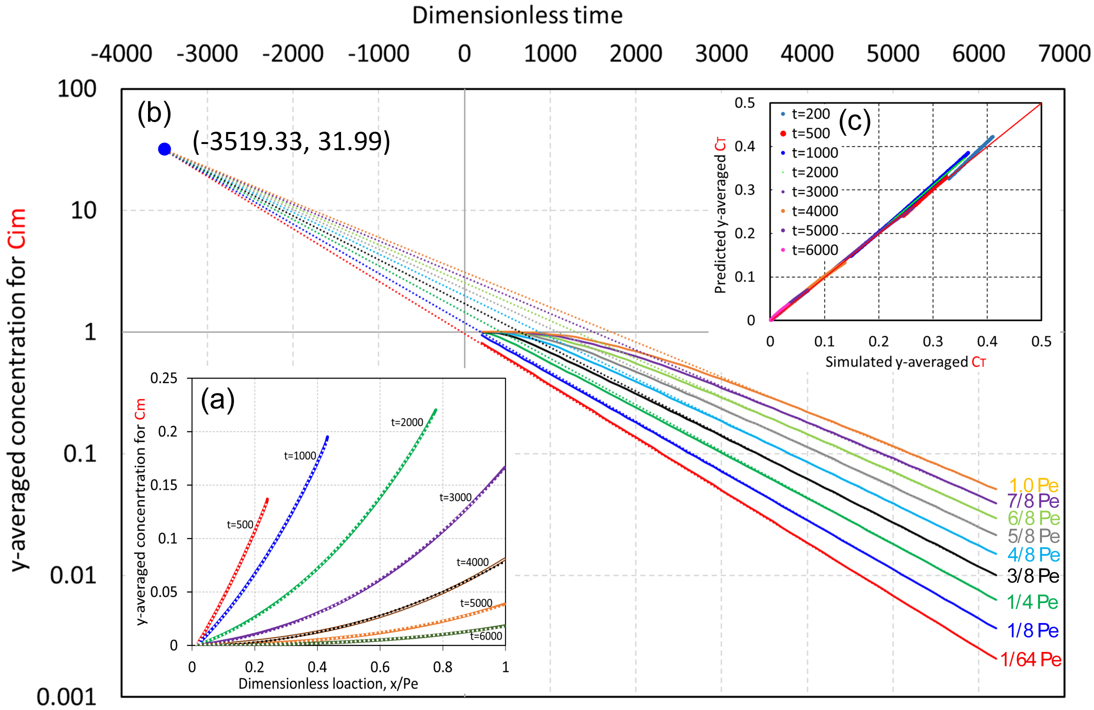

Figure 7: Prediction of y-averaged concentration profiles behind the finger trailing fronts. (a) C_m, (b) C_{im}, and (c) simulated vs. predicted C_T. In plot (a), solid lines are from nonlinear numerical simulations, and dots are from curve fitting. They are nearly overlapped. In plot (c), a large number of data points are matched.

tain the simple empirical models for y-averaged C_m ($\overline{C_m^y}$) and C_{im} ($\overline{C_{im}^y}$) separately in the following.

Behind the finger trailing front, the $\overline{C_m^y}$ exhibits a second-order polynomial relation with location along the flow direction, as shown in Fig. 7a. We thus assume the following relation,

$$\overline{C_m^y} = \alpha_1(t) \cdot \left(\frac{x}{Pe} - x_0\right)^2 + \alpha_2(t) \cdot \left(\frac{x}{Pe} - x_0\right) \tag{14}$$

where $x_0 = Pe/64$ is the location of initial front, and $x \in [x_0, Pe]$ which is from x_0 to outlet of the domain. $\alpha_1(t)$ and $\alpha_2(t)$ are coefficients and dependent on time; $\alpha_1(t) = 0.8184e^{-5.903\times10^{-4}t}$ and $\alpha_2(t) = 0.8047e^{-1.108\times10^{-3}t}$. More details on determination of their values can be found in Appendix B.

The $\overline{C_{im}^y}$ seems to vary differently with $\overline{C_m^y}$ in Fig. 5. However, we found that at a *fixed* location in the flow direction, the $\overline{C_{im}^y}$ decreases linearly with time in the semi-log scale in the certain time interval when it is located behind finger trailing front, represented by the dotted lines Fig. 7b. Specifically, the $\overline{C_{im}^y}$ at initial front $x_0 = Pe/64$ decreases linearly with time in the whole displacement processes, while away from it the linear regime for $\overline{C_{im}^y}$ tends to happen at later times. Interesting, all the straight lines meet at the same point (-3519.33, 31.99). Therefore, the y-averaged concentration for C_{im} can be predicted using the equation,

$$log(\overline{C_{im}^y}) = \beta_1 \cdot (t - t_0) + \beta_2 \tag{15}$$

where $t_0 = -3519.33$, $\beta_2 = log(31.99) = 1.5050$. β_1 is a function of x/Pe and given by

$$\beta_1\Big(\frac{x}{Pe}\Big) = -6.8893 \times 10^{-5} \cdot \Big(\frac{x}{Pe} - x_0\Big)^2 + 2.0865 \times 10^{-4}\Big(\frac{x}{Pe} - x_0\Big) - 4.2965 \times 10^{-4} \quad (16)$$

More details for the determination of β_1 can be found in Appendix C.

The y-averaged overall concentration in the porous media $\overline{C_T^y}$ can therefore be obtained by $\overline{C_T^y} = f \cdot \overline{C_m^y} + (1-f) \cdot \overline{C_{im}^y}$. As shown in Fig. 7c, the predicted $\overline{C_T^y}$ fits well with that from the nonlinear numerical simulations in the whole displacement processes. This simpler model can therefore be used to accurately predict the y-averaged concentrations for C_m, C_{im} and C_T for the region behind finger trailing fronts. Note that our simple model incorporates the effects of fingering instabilities on the y-averaged concentration profiles and cannot be obtained by an analytical approach.

3.3 Remaining NAPLs and Flow Regimes

Besides the trapped NAPLs in the region behind the finger trailing fronts, it is also important to characterize the variations of remaining NAPLs with time in the whole domain and in swept area and how they are affected by the fingering instabilities.

Figure 8a depicts the averaged remaining concentration with time for C_m, C_{im}, and C_T. The curves without symbols represent the averaged remaining NAPLs in the *whole* domain, while those with symbols represent the averaged remaining NAPLs in an *assumed stable swept area* as if the displacement is stable. The concentration contour 0.99 is used to define the front of such assumed stable swept area by injected fluids. It is obvious that the remaining NAPLs in the whole domain gradually decrease as the displacement continue. However, in the assumed stable swept area, the remaining NAPLs vary non-monotonically with time. After breakthrough, the curves of these two kinds of remaining NAPLs are overlapped.

Figure 8b depicts the cleanup rate of remaining NAPLs in the *whole* domain, while the corresponding cleanup rate in *the stable swept area* is not plotted as it shows a lot of oscillations between any two time intervals. The overall cleanup rate of C_T is constant before breakthrough time $t = 640$ because of the constant injection rate and because only NAPLs are produced in this period. Once breakthrough happens, the cleanup rate of C_T decreases substantially. The cleanup rates of C_m and C_{im} behaves differently. At the beginning, the cleanup rate of C_m is the highest but decreases slightly. It is about two orders higher than that of C_{im} because of the free fluid flows in well-connected pore network. While the cleanup rate of C_{im} is very low at the beginning. One reason is that the trapped NAPLs in dead-end pores cannot be produced directly at outlet. Another reason is that the dissolution rate is still low due to less contact with injected fluids. However, with time, the cleanup rate of C_{im} increases because more NAPLs will dissolve to adjacent well-connected pores thus be flushed. At later times, the cleanup rate of C_{im} reaches the maximum and then decreases, indicating that the DF has fully developed at this time. According to the fingering dynamics and variations of cleanup of NAPLs, we divide the full 'life cycle' displacement processes into six regimes.

- Regime I: diffusion-dominated regime, $t \in [0, 90)$.
  This is similar with the traditional VF without dead-end pore effects. The flows are stable and fingering instability has not yet fully developed. Because of this stable flows, the sweep efficiency of injected fluids increases, thus the averaged remaining concentration of C_m in the swept area decreases, as shown in Fig. 8a (red curve with star symbols). At $t = 90$, the fingers become obvious and the averaged remaining NAPL C_T reaches a local minimum value with about 60% NAPLs in the stable swept area (blue curve with solid symbols at $t = 90$).
- Regime II: convection-dominated regime, $t \in [90, 640)$.

(a)

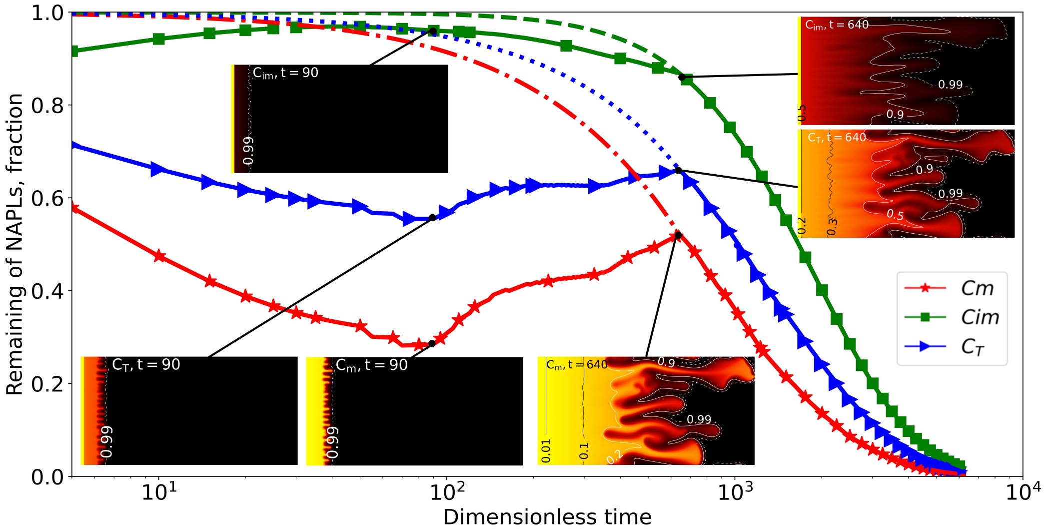

(b)

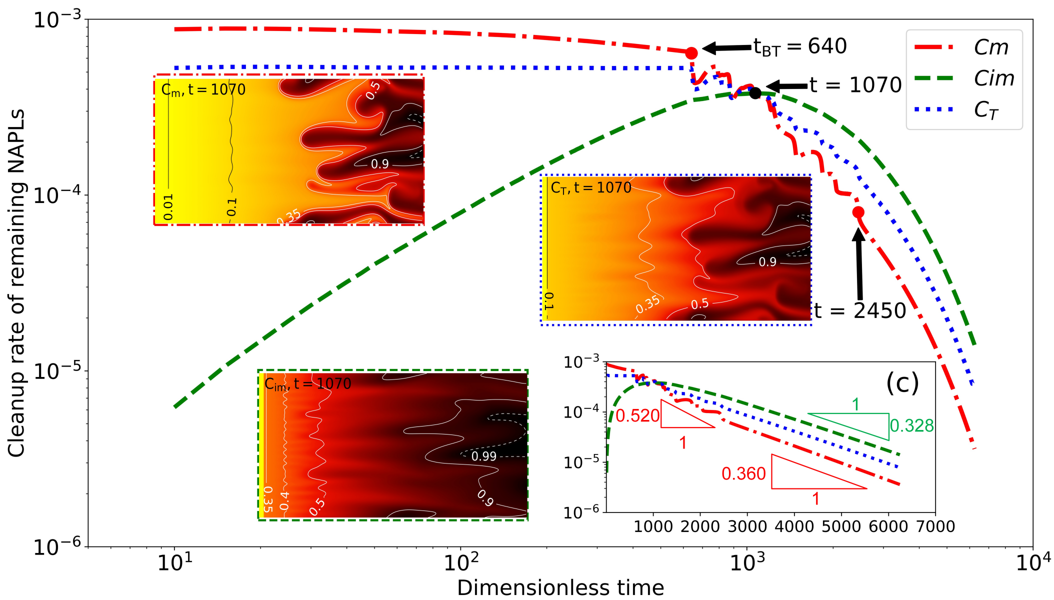

Figure 8: Variations of remaining NAPLs at $Pe = 2000$, $f = 0.6$, and $Da = 0.001$. (a) remaining NAPLs in the *whole* domain (curves without symbols) and in *swept area* (curves with symbols), (b) cleanup rate of remaining NAPLs in the *whole* domain.

In this regime, both VF in well-connected pore network and DF in dead-end pore network have fully developed to be large fingers. Because of the increasingly unstable flows, the averaged remaining C_m in the assumed stable swept area increases with time, while the corresponding C_{im} slightly decreases due to more dissolution. When breakthrough happens at the end of this regime, the corresponding averaged remaining C_{im} and C_T in the whole domain are about 0.85 and 0.62, respectively. Thus, most of the NAPLs are still trapped and uncleaned *at* breakthrough. This also indicates that investigation of the fingering dynamics and performances of NAPL cleanup *after* breakthrough are extremely important, in comparison with most previous studies where the main focus is the fingering dynamics *till* breakthrough. Note that only pure NAPLs are produced during regimes I and II.

- Regime III:VF production regime, $t \in [640, 1070)$.
  Starting from this regime, the remaining NAPLs in the assumed stable swept area and in the whole domain are the same. The cleanup rate of C_m shows strong fluctuations (red curve in Fig. 8b) because of the production of the finger-like injected fluids at outlet. However, the cleanup rate of C_{im} continues to slightly increase in this regime because of the increasing contacts for trapped NAPLs in dead-end pores with the injected fluids in adjacent pores and the still large amount of NAPLs in dead-end pores. With time, the difference on their cleanup rate tends to be smaller and become the same at the end of this regime.
- Regime IV: VF-to-DF transition regime, $t \in [1070, 2450)$.
  As more and more NAPLs in the well-connected pores are produced, the cleanup rate of C_m continues to decrease, while that of C_{im} also begins to decrease after reaching a maximum value at the end of last regime. In well-connected pore network, the VF instability can still strongly affect the cleanup of NAPLs, as indicated by the fluctuations of red curve in Fig. 8c. However, its influences on cleanup of C_m decreases with time, as indicated by the concentration profiles for C_m at $t = 1070$ and $t = 2450$ in Figs. 8b and 9a. Once the last VF trailing front reaches the outlet at $t = 2450$ at the end of this regime (see Fig. 9a), its influences become weak. Figure 8c shows the cleanup rate of C_m decreases with a slope of 0.520 on semi-log scale during regimes III and IV. The influences of DF lags behind that of VF. For one thing, its cleanup rate just starts to decrease at the beginning of this regime. For another, at the end of this regime, the DF is still strongly unstable and affect the spatial distribution of NAPLs (see Figs. 9b and 9c). Similar to C_m, the cleanup rate of C_{im} decreases fast with time.
- Regime V: DF-dominated regime, $t \in [2450, 5000)$.
  After the last VF trailing front reaches outlet, nearly all NAPLs that initially saturate the well-connected pores are produced. The remaining NAPLs in well-connected pores are mostly from the trapped NAPLs that dissolve from dead-end pores. The spatial distribution of C_m and C_T is thus dominated by the DF instability. At the beginning of this regime at $t = 2450$ in Fig. 9b, the C_{im} is still above 0.5 on average at the outlet, and the strong DF instability can be clearly observed. With time, its influences decay. At $t = 5000$, a much later time after breakthrough, the DF is much weaker, as depicted in Fig. 10b. Although the VF and DF instabilities clearly affect the NAPL distributions as indicated by the concentration contours, their cleanup rates seem to decrease linearly with time on the semi-log scale in Fig. 8c. The slopes for C_m and C_{im} are 0.360 and 0.328, respectively. This is also why our simple empirical models can be developed to predict the y-averaged concentration profiles for the *unstable* flows behind the finger trailing front.
- Regime VI: Pseudo-stable regime, $t \in [5000, \infty)$.
  If the displacement process is long enough, the NAPL concentration at the outlet is low enough. Although slightly unstable flows can still be observed as shown in Fig. 10, they may be not important. Note that the importance of fingering instabilities in this regime also depends on the value of regulatory limit for NAPL concentrations. A lower level of NAPL concentration in produced fluids needs longer

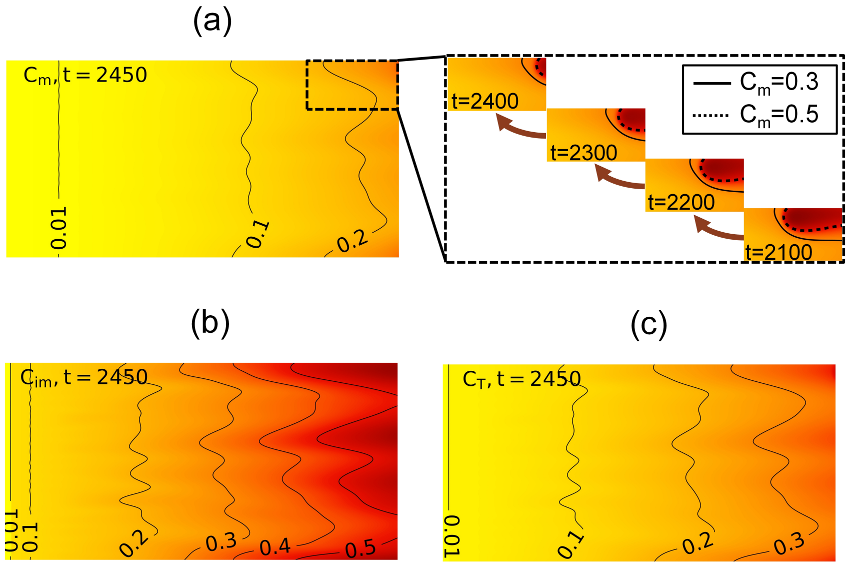

Figure 9: Concentration profiles at time $t = 2450$ for C_m, C_{im}, and C_T at $f = 0.6$ and $Da = 0.001$.

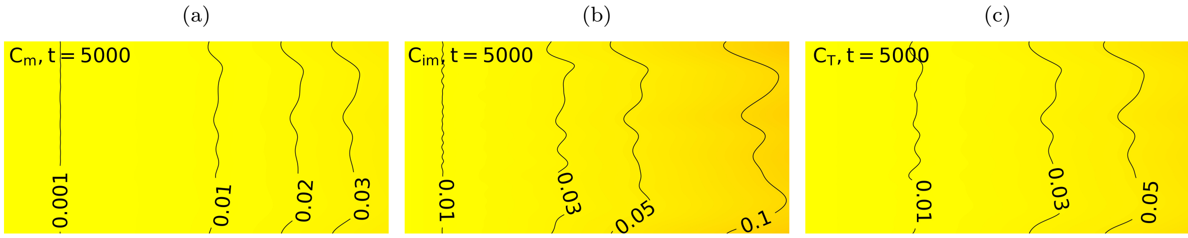

Figure 10: Concentration profiles at time $t = 5000$ for (a) C_m, (b) C_{im}, and (c) C_T at $f = 0.6$ and $Da = 0.001$.

time displacement and more accurate characterization of fingering instabilities at later times. The effects of fingering instabilities will be eventually disappear and negligible as the displacements continue. We therefore refer this regime to pseudo-stable regime.

3.4 Distribution of Spatial Cleanup Rate

In the above, we analyzed the effects of fingering instabilities on the *temporal* variations of the NAPLs for C_m, C_{im}, and C_T. We are also interested in how the fingering instabilities affect the *spatial* cleanup rate of the trapped NAPLs in dead-end pore network. To conduct this analysis, we first define the scaled cleanup rate $(\frac{\partial C_{im}}{\partial t})_s$ as,

$$\left(\frac{\partial C_{im}}{\partial t}\right)_s = -\frac{\frac{\partial C_{im}}{\partial t}}{Da} = C_{im} - C_m \tag{17}$$

Once the concentration profiles are obtained from nonlinear numerical simulations at different times, the $(\frac{\partial C_{im}}{\partial t})_s$ can be easily calculated and plotted. To better show the spatial cleanup distribution $\frac{\partial C_{im}}{\partial t}$, we use an non-uniform color map, the jet color map. Note that such non-uniform color map may cause confusions for analyzing flow dynamics (Borland

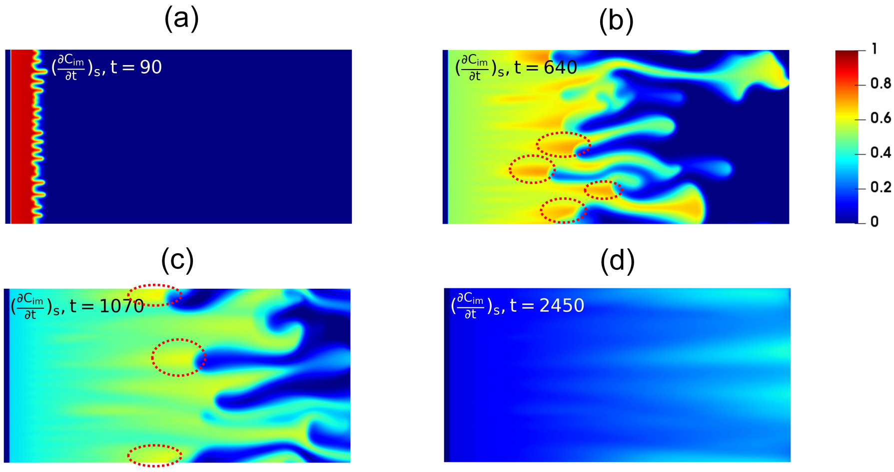

Figure 11: The changes of $(\partial C_{im}/\partial t)_s$ at different times for $f = 0.6$ and $Da = 0.001$.

& Taylor, 2007), but it is quite helpful for this purpose by enhancing the contrasts of spatial cleanup rates.

Figure 11 depicts the $(\frac{\partial C_{im}}{\partial t})_s$ and its variations with time. In swept area, the $(\frac{\partial C_{im}}{\partial t})_s$ decreases with time. At a later time, for example $t = 640$, the finger tips usually have higher C_{im} cleanup rate, as the injected fluids contact with the fresh NAPLs in the downstream of the domain. However, a comparison of the concentration profiles with their corresponding $(\frac{\partial C_{im}}{\partial t})_s$ at the same time indicates that the highest cleanup rate of C_{im} is located slightly behind the VF trailing fronts, as shown by the circles in Fig. 11b and 11c. These locations also correspond to those near the DF trailing fronts and between two neighbor dissolution fingers, as shown in the concentration fields in Fig. 8. These locations still have high trapped NAPL in dead-end pores and their adjacent well-connected pores are swept by injected fluids. After a long-time displacement at $t = 2450$, the C_{im} at upstream of the domain decreases very slowly, depicted by the blue color in Fig. 11d. Since the whole domain has been swept after the VF trailing front reaches the boundary, the cleanup rate of C_{im} mainly depends on the spatial distribution of remaining NAPLs. The locations with higher trapped NAPLs typically have larger values of $(\frac{\partial C_{im}}{\partial t})_s$.

4 Conclusions

In this study, the fingering instabilities and their effects on the cleanup of NAPLs were investigated in a homogeneous porous medium with non-negligible dead-end pores. Highly accurate nonlinear numerical simulations showed that the dissolution of trapped NAPLs from dead-end pores to adjacent well-connected pores plays a role in affecting fingering instabilities and the efficiency of cleanup of NAPLs in the porous media. Several important findings were reported for the first time. The main conclusions are drawn as follows.

We identified for the first time the dissolution fingering (DF) mechanism formed in dead-end pore network in porous media during *miscible* displacements. This new DF instability is fundamentally different with the classic viscous fingering (VF) mechanism and the DF reported in *immiscible* displacements. It is induced by the VF, and its structures are determined by the accumulated flush over time along the preferential flow paths in well-connected pore network. In return, the DF as well as the trapped NAPLs in dead-end pore network also affects the VF dynamics by slow dissolution, resulting in higher NAPL concentration in swept area of injected fluids. The VF and DF are therefore coupled, interact, and determine the miscible displacement efficiency together.

Based on nonlinear numerical simulations, we developed simple models to predict the y-averaged concentrations in dead-end pores, well-connected pores, and the whole porous media. The predicted results can perfectly fit the simulated results for the region behind the finger trailing front in miscible displacements.

According to the temporal variations of fingering dynamics and the remaining NAPLs, we divide the full 'life cycle' displacements into six regimes: (I) diffusion-dominated region; (II) convection-dominated regime; (III) VF production regime; (IV) VF-to-DF transition regime; (V) DF-dominated regime; and (VI) pseudo-stable regime. While most of the previous studies on fingering instabilities focused on the first two regimes, our research showed that the last four regimes are equally important in groundwater remediation in the efforts to reduce the NAPL concentration to the regulatory limit.

We also identified the spatial variations of cleanup rate of trapped NAPLs in dead-end pore network. The largest cleanup rate of trapped NAPLs are typically located behind the finger trailing front where the injected fluids have just flushed the well-connected pore but there is still a large amount of trapped NAPLs in dead-end pores.

Note that the above analysis is based on the fixed f, Da, Pe, and R. Examining their impacts on both the VF and DF instabilities as well as the cleanup of NAPLs in porous media with dead-end pores is also important and will be conducted in the future work. This research will have catalytic impacts for researchers to re-examine a variety factors, such as heat transfer, inertia, heterogeneity, reaction, and miscibility, on fingering dynamics in this specific porous media. The model presented in this work can be extended to the similar displacements in other applications, such as CO_2 sequestration, enhanced oil recovery, geothermal recovery, drug delivery, and chromatographic separation.

Acknowledgments

Financial support for this study is provided by the startup and the Matejek Family Faculty Fellow in the Department of Petroleum Engineering at Texas Tech University (TTU). The authors would also like to thank the TTU's High Performance Computing Center (HPCC) for providing computational resources. The authors also thank Amber McCord and Bowen Zhang for helping with the animations in Supplementary information.

Data Statement

All data used for concentration fields, y-averaged concentration profiles, location of finger trailing front, variations of remaining NAPL and its cleanup rate, and spatial cleanup rate distributions may be accessed at: https://doi.org/10.18738/T8/JJ1WR9.

Nomenclature

Abbreviations

DF	Dissolution fingering
EOR	Enhanced Oil Recovery
NAPLs	Non-aqueous phase liquids
VF	Viscous fingering

Symbols

α	The first-order mass transfer rate coefficient for NAPL dissolution from dead-end pores to well-connected pores
α_i	Coefficients for $\overline{C_m^y}$ $(i = 1, 2)$
β_i	Coefficients for $\overline{C_{im}^y}$ $(i = 1, 2)$
Δt	Time step
$\mathbf{u}$	Velocity vector, $\mathbf{u} = (u, v)$
μ	Viscosity

ω	Vorticity
$\overline{C_m^y}$	y-averaged concentration in well-connected pore network
$\overline{C_{im}^y}$	y-averaged concentration in dead-end pore network
ϕ	Porosity
ψ	Streamfunction
A	Aspect ratio of the domain
C	Concentration in porous media without dead-end pores
C_m	Concentration in well-connected pore network in porous media
C_{im}	Concentration in dead-end pore network in porous media
C_T	Overall concentration in porous media with dead-end pores
D	Diffusion coefficient
Da	Damköhler number
f	Fraction of the well-connected pores in porous media (the fraction of dead-end pore is therefore $1-f$)
k	Permeability
L_x	Length of domain
L_y	Width of domain
N_x	Grid size in x direction
N_y	Grid size in y direction
P	Pressure
Pe	Péclet number
R	Log viscosity ratio
t	Time
u	Velocity in x direction
v	Velocity in y direction
x	Location in flow direction
x_0	Location of initial interface
x_t	Location of finger trailing front with time
y	Location in transverse direction

Appendices

A Alternating-direction implicit (ADI) method

The fully implicit ADI method is used for time advancement. First, Eq. (8) is discretized in x direction from t to $t+\Delta t/2$:

$$f\frac{C^*_{m(i,j)}-C^n_{m(i,j)}}{\Delta t/2}+Da(1-f)\left(C^*_{m(i,j)}-C^n_{im(i,j)}\right)+\left[\left(\frac{\partial\psi^n}{\partial y}\right)_{i,j}+1\right]\frac{C^*_{m(i+1,j)}-C^*_{m(i-1,j)}}{2\Delta x}$$
$$-\left(\frac{\partial\psi^*}{\partial x}\frac{\partial C^n_m}{\partial y}\right)_{i,j}=\frac{C^*_{m(i+1,j)}-2C^*_{m(i,j)}+C^*_{m(i-1,j)}}{\Delta x^2}+\left(\frac{\partial^2C^n_m}{\partial y^2}\right)_{i,j} \tag{A.1}$$

where $i\in[1,N_x]$ and $j\in[1,N_y]$. Superscripts n and * symbol represent the concentration at time t and $t+\Delta t/2$, respectively. Re-arranging Eq. (A.1), we get

$$\left[-\frac{(\frac{\partial\psi^n}{\partial y})_{i,j}+1}{2\Delta x}-\frac{1}{\Delta x^2}\right]C^*_{m(i-1,j)}+\left[\frac{2f}{\Delta t}+\frac{2}{\Delta x^2}+Da(1-f)\right]C^*_{m(i,j)}$$
$$+\left[\frac{(\frac{\partial\psi^n}{\partial y})_{i,j}+1}{2\Delta x}-\frac{1}{\Delta x^2}\right]C^*_{m(i+1,j)}=\frac{2f}{\Delta t}C^n_{m(i,j)}+\left(\frac{\partial\psi^*}{\partial x}\frac{\partial C^n_m}{\partial y}\right)_{i,j}+\left(\frac{\partial^2C^n_m}{\partial y^2}\right)_{i,j}+Da(1-f)C^n_{im(i,j)} \tag{A.2}$$

$\frac{\partial\psi^*}{\partial x}$ is approximated using the sixth-order finite difference method in real space, while $\frac{\partial C^n_m}{\partial y}$ and $\frac{\partial^2C^n_m}{\partial y^2}$ are calculated in Hartley space and then transformed to real space.

When $i = 1$, $C_{m(0,j)} = 0$ at the left boundary (inlet). Equation (A.2) then takes the form of,

$$\begin{aligned}
&\left[\tfrac{2f}{\Delta t} + \tfrac{2}{\Delta x^2} + Da(1-f)\right] C^*_{m(i,j)} + \left[\tfrac{(\frac{\partial \psi^n}{\partial y})_{i,j}+1}{2\Delta x} - \tfrac{1}{\Delta x^2}\right] C^*_{m(i+1,j)} \\
&= \tfrac{2f}{\Delta t} C^n_{m(i,j)} + (\tfrac{\partial \psi^*}{\partial x}\tfrac{\partial C^n_m}{\partial y})_{i,j} + (\tfrac{\partial^2 C^n_m}{\partial y^2})_{i,j} + Da(1-f) C^n_{im(i,j)}
\end{aligned} \tag{A.3}$$

When $i = N_x$ at the right boundary (outlet), the fluids are assumed to flow freely. A ghost cell is added for $i = N_x + 1$, and its concentration is extrapolated using its two upstream neighbour grid points, thus $C^*_{m(N_x+1,j)} = 2C^*_{m(N_x,j)} - C^*_{m(N_x-1,j)}$. Therefore, when $i = N_x$, Eq. (A.2) takes the form of,

$$\begin{aligned}
&\left[-\tfrac{(\frac{\partial \psi^n}{\partial y})_{i,j}+1}{2\Delta x} - \tfrac{1}{\Delta x^2} - \left(\tfrac{(\frac{\partial \psi^n}{\partial y})_{i,j}+1}{2\Delta x} - \tfrac{1}{\Delta x^2}\right)\right] C^*_{m(i-1,j)} \\
&+ \left[\tfrac{2f}{\Delta t} + \tfrac{2}{\Delta x^2} + Da(1-f) + 2\left(\tfrac{(\frac{\partial \psi^n}{\partial y})_{i,j}+1}{2\Delta x} - \tfrac{1}{\Delta x^2}\right)\right] C^*_{m(i,j)} \\
&= \tfrac{2f}{\Delta t} C^n_{m(i,j)} + (\tfrac{\partial \psi^*}{\partial x}\tfrac{\partial C^n_m}{\partial y})_{i,j} + (\tfrac{\partial^2 C^n_m}{\partial y^2})_{i,j} + Da(1-f) C^n_{im(i,j)}
\end{aligned} \tag{A.4}$$

The resulting tridiagonal system of equations is then solved for C^*_m using the Thomas matrix algorithm (Hoffman & Frankel, 2001).

Once C^*_m is obtained, C^*_{im} is calculated implicitly at time $t + \Delta t/2$,

$$\frac{C^*_{im} - C^n_{im}}{\Delta t/2} = Da(C^*_m - C^*_{im}) \tag{A.5}$$

Thus,

$$C^*_{im} = \frac{1}{1 + \frac{\Delta t \cdot Da}{2}} \left(\frac{\Delta t \cdot Da}{2} C^*_m + C^n_{im} \right) \tag{A.6}$$

This process is iterated until convergence for C_m is achieved with tolerance 1.0e-5. The C^*_m and C^*_{im} are then used for time from $t + \Delta t/2$ to $t + \Delta t$ in y direction. The process is similar to the above procedure and will not be discussed here. The difference is that the periodic boundary condition is used for the y direction. More details about ADI method for the simulations of classic VF dynamics can be found in Islam and Azaiez (2005) and Yuan et al. (2017b). Once C_m and C_{im} at time t+Δt are obtained, the overall concentration C_T can be calculated by $C_T = f \cdot C_m + (1-f) \cdot C_{im}$.

B Determination of $\boldsymbol{\alpha_1(t)}$ and $\boldsymbol{\alpha_2(t)}$

The values of $\alpha_1(t)$ and $\alpha_2(t)$ in Eq. (Eq:alpha12) in section 3.2 can be determined by curve fitting for C_m behind fingering trailing front. Here, we use a time interval 100 and vary time from $t = 200$ to $t = 6200$ so that a total of 32 points are used for each coefficient. The dots in Fig. B.1 show the general trend, and the curves are from curve fitting. The $\alpha_1(t)$ and $\alpha_2(t)$ show very good exponential relation with dimensionless time.

C Determination of $\boldsymbol{\beta_1}$

To obtain the dependency of β_1 on location in Eq. (16), we first determine the slopes of dotted curves in Fig. 7b but with a location interval $Pe/32$ in the flow direction. Therefore, 32 data points are obtained, as shown by the symbols in Fig. C.1. The expression of $\beta_1(x/Pe)$ is then obtained by a simple curve fitting. This relation is valid for the region behind the finger trailing front.

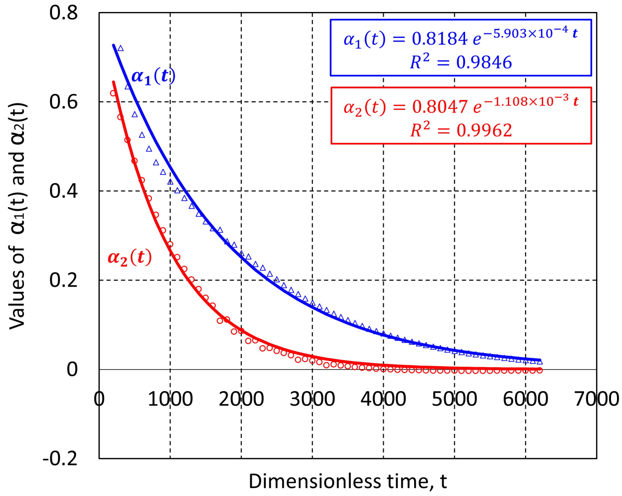

Figure B.1: Determination of $\alpha_1(t)$ and $\alpha_2(t)$.

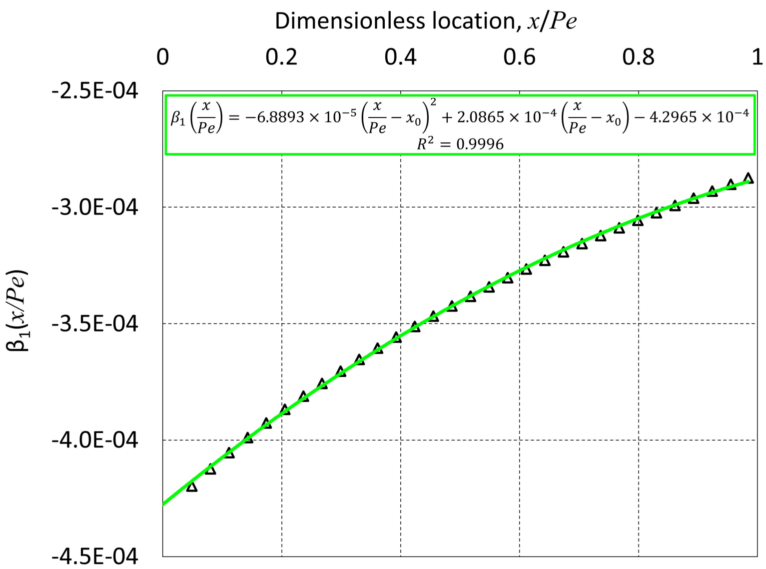

Figure C.1: Determination of $\beta_1(x/Pe)$.

References

Al-Housseiny, T., Tsai, P., & Stone, H. (2012). Control of interfacial instabilities using flow geometry. *Nature Physics*, *8*, 747–750. doi: https://doi.org/10.1038/nphys2396

Ali, M. A., Dzombak, D. A., & Roy, S. B. (1995). Assessment of in situ solvent extraction for remediation of coal tar sites: Process modeling. *Water Environment Research*, *67*(1), 16–24.

Almarcha, C., Trevelyan, P. M. J., Grosfils, P., & De Wit, A. (2010). Chemically driven hydrodynamic instabilities. *Physical Review Letters*, *104*, 044501. doi: https://doi.org/10.1103/PhysRevLett.104.044501

Babaei, M., & Islam, A. (2020). Convective-reactive co2 dissolution in aquifers with mass transfer with immobile water. *Water Resources Research*, *54*, 9585–9604. doi: https://doi.org/10.1029/2018WR023150

Bai, M., Bouhroum, A., Civan, F., & Roegiers, J.-C. (1995). Journal of petroleum science and engineering. *SPE Journal*, *14*(1), 65–78. doi: https://doi.org/10.1016/0920-4105(95)00024-0

Baker, L. (1977). Effects of dispersion and dead-end pore volume. *SPE Journal*, *17*(3), 219–227. doi: https://doi.org/10.2118/5632-PA

Borland, D., & Taylor, R. (2007). Rainbow color map (still) considered harmful. *IEEE Computer Graphics and Applications*, *27*(2), 14–17.

Bretz, R. E., & Orr, F. M. (1987). Interpretation of miscible displacements in laboratory cores. *SPE Reservoir Engineering*, *2*(4), 492–500. doi: https://doi.org/10.2118/14898-PA

Bretz, R. E., Welch, S. L., Morrow, N. R., & Orr, F. M. (1986). *Mixing during two-phase, steady-state laboratory displacements in sandstone cores.* Paper presented at the SPE Annual Technical Conference and Exhibition, New Orleans, Louisiana, USA. doi: https://doi.org/10.2118/15389-MS

Brigham, W. E. (1974). Mixing equations in short laboratory cores. *SPE Journal*, *14*(1), 91–99. doi: https://doi.org/10.2118/4256-PA

Chen, C.-Y., & Eckart, M. (1998). Miscible porous media displacements in the quarter five-spot configuration. part 1. the homogeneous case. *Journal of Fluid Mechanics*, *371*(5), 233–268. doi: https://doi.org/10.1017/S0022112098002195

Coats, K. H., & Smith, B. D. (1964). Dead-end pore volume and dispersion in porous media. *SPE Journal*, *4*(1), 73–84. doi: https://doi.org/10.2118/647-PA

De Wit, A. (2020). Chemo-hydrodynamic patterns and instabilities. *Annual Review of Fluid Mechanics*, *52*(1), 531–555. doi: https://doi.org/10.1146/annurev-fluid-010719-060349

Escala, D. M., De Wit, A., Carballido-Landeira, J., & Muñuzuri, A. P. (2019). Viscous fingering induced by a ph-sensitive clock reaction. *Langmuir*, *35*(11), 4182–4188. doi: https://doi.org/10.1021/acs.langmuir.8b03834

Ghesmat, K., & Azaiez, J. (2008). Viscous fingering instability in porous media: Effect of anisotropic velocity-dependent dispersion tensor. *Transport in Porous Media*, *73*(3), 297–318. doi: https://doi.org/10.1007/s112420079171y

Gooya, R., Silvestri, A., Moaddel, A., Andersson, M. P., Stipp, S. L. S., & Sørensen, H. O. (2019). Unstable, super critical co_2–water displacement in fine grained porous media under geologic carbon sequestration conditions. *Scientific Reports*, *9*(11272). doi: https://doi.org/10.1038/s41598-019-47437-5

Hoffman, J. D., & Frankel, S. (2001). Numerical methods for engineers and scientists. In 2nd Ed. (2nd ed.). New York: CRC Press. doi: https://doi.org/10.1201/9781315274508

Imhoff, P. T., & Miller, C. T. (1996). Dissolution fingering during the solubilization of nonaqueous phase liquids in saturated porous media: 1. model predictions. *Water Resources Research*, *32*(7), 1919–1928. doi: https://doi.org/10.1029/96WR00602

Imhoff, P. T., Thyrum, G. P., & Miller, C. T. (1996). Dissolution fingering during the solubilization of nonaqueous phase liquids in saturated porous media: 2. experimental observations. *Water Resources Research*, *32*(7), 1929–1942. doi: https://doi.org/10.1029/96WR00601

Islam, M., & Azaiez, J. (2005). Fully implicit finite dierence pseudo-spectral method for simulating high mobility-ratio miscible displacements. *International Journal for Numerical Methods in Fluids*, *47*, 161–183. doi: https://doi.org/10.1007/s11242-010-9542-7

Islam, M., & Azaiez, J. (2010). Miscible thermo-viscous fingering instability in porous media. part 2: Numerical simulations. *Transport in Porous Media*, *84*, 845–861. doi: https://doi.org/10.1007/s11242-010-9542-7

Jasti, J. K., Vaidya, R. N., & Fogler, H. S. (1988). Capacitance effects in porous media. *SPE Reservoir Engineering*, *3*(4), 1207–1214. doi: 10.2118/16707-PA

Jha, B., Cueto-Felgueroso, L., & Juanes, R. (2011). Quantifying mixing in viscously unstable porous media flows. *Physical Review E*, *84*, 066312. doi: https://doi.org/10.1103/PhysRevE.84.066312

Kahler, D. M., & Kabala, Z. J. (2016). Acceleration of groundwater remediation by deep sweeps and vortex ejections induced by rapidly pulsed pumping. *Water Resources Research*, *52*, 3930–3940. doi: https://doi.org/10.1002/2015WR017157

Kar, A., Chiang, T., Rivera, I. O., Sen, A., & Velegol, D. (2015). Enhanced transport into and out of dead-end pores. *ACS Nano*, *9*(1), 746–753. doi: https://doi.org/10.1016/j.ces.2018.01.007

Karadimitriou, N. K., Joekar-Niasar, V., Babaei, M., & Shore, C. A. (2016). Critical role of the immobile zone in non-fickian two-phase transport: A new paradigm. *Environmental Science & Technology*, *50*, 4384–4392. doi: https://doi.org/10.1021/acs.est.5b05947

Lake, L. W. (1989). *Enhanced oil recovery* (1st ed.). Englewood Cliffs: Prentice-Hall Inc.

Lele, S. K. (1992). Compact finite difference schemes with spectral-like resolution. *Journal of Computational Physics*, *103*(1), 16–42. doi: https://doi.org/10.1016/0021-9991(92)90324-R

Lifton, V. A. (2016). Microfluidics: an enabling screening technology for enhanced oil recovery (eor). *Lab on a Chip*, *16*, 1777. doi: https://doi.org/10.1039/c6lc00318d

Mayfield, K. J., Shalliker, R. A., Catchpoole, H. J., Sweeney, A. P., Wong, V., & Guiochon, G. (2005). Viscous fingering induced flow instability in multidimensional liquid chromatography. *Journal of Chromatography A*, *1080*(2), 124–131. doi: https://doi.org/10.1016/j.chroma.2005.04.093

Meng, X., & Guo, Z. (2016). Localized lattice boltzmann equation model for simulating miscible viscous displacement in porous media. *International Journal of Heat and Mass Transfer*, *100*(2), 767–778. doi: https://doi.org/10.1016/j.ijheatmasstransfer.2016.04.095

Mishra, M., Martin, M., De Wit, A., Wong, V., & Guiochon, G. (2007). Miscible viscous fingering with linear adsorption on the porous matrix. *Physics of Fluids*, *19*(7), 073101. doi: https://doi.org/10.1063/1.2743610

Nijjer, J., Hewitt, D., & Neufeld, J. (2018). The dynamics of miscible viscous fingering from onset to shutdown. *Journal of Fluid Mechanics*, *837*, 520–545.

Norouzi, M., & Shoghi, M. R. (2014). A numerical study on miscible viscous fingering instability in anisotropic porous media. *Physics of Fluids*, *26*(8), 084102. doi: https://doi.org/10.1063/1.4891228

Orr, F. M., & Taber, J. J. (1984). Use of carbon dioxide in enhanced oil recovery. *Science*, *224*, 563–569. doi: https://doi.org/10.1126/science.224.4649.563

Piquemal, J. (1993). On the modelling conditions of mass transfer in porous media presenting capacitance effects by a dispersion-convection equation for the mobile fluid and a diffusion equation for the stagnant fluid. *Transport in Porous Media*, *10*, 271–283. doi: https://doi.org/10.1007/BF00616813

Rabbani, H. S., Or, D., Liu, Y., Lai, C.-Y., Lu, N. B., Datta, S. S., … Shokri, N. (2018). Suppressing viscous fingering in structured porous media. *Proceedings of the National Academy of Sciences*, *115*(19), 4833–4838. doi: https://doi.org/10.1073/pnas.1800729115

Rana, C., Pramanik, S., Martin, M., De Wit, A., & Mishra, M. (2019). Influence of langmuir adsorption and viscous fingering on transport of finite size samples in porous media. *Physical Review Fluids*, *4*(10), 104001. doi: https://doi.org/10.1103/physrevfluids.4.104001

Riaz, A., Hesse, M., Tchelepi, H. A., & Orr, F. M. (2006). Onset of convection in a gravitationally unstable diffusive boundary layer in porous media. *Journal of Fluid Mechanics*, *548*, 87–111. doi: https://doi.org/10.1017/S0022112005007494

Roy, S. B., Dzombak, D. A., & Ali, M. A. (1995). Assessment of in situ solvent extraction for remediation of coal tar sites: Column studies. *Water Environment Research*, *67*(1), 4–15.

Sabet, N., Hassanzadeh, H., & Abedi, J. (2020). Dynamics of viscous fingering in porous media in the presence of in situ formed precipitates and their subsequent deposition. *Water Resources Research*, *56*, e2019WR027042. doi: https://doi.org/doi.org/10.1029/2019WR027042

Sajjadi, M., & Azaiez, J. (2013). Scaling and unified characterization of flow instabilities in layered heterogeneous porous media. *Physical Review E*, *88*, 033017. doi: https://doi.org/10.1103/PhysRevE.88.033017

Sajjadi, M., & Azaiez, J. (2014). *Improvement of sweep efficiency of miscible displacement processes in heterogeneous porous media.* Paper presented at the SPE Heavy Oil Conference-Canada, Calgary, Alberta, Canada. doi: https://doi.org/10.2118/170155-MS

Sajjadi, M., & Azaiez, J. (2016). Hydrodynamic instabilities of flows involving melting in under-saturated porous media. *Physics of Fluids*, *28*(3), 033104. doi: https://doi.org/10.1063/1.4943596

Salter, S., & Mohanty, K. (1982). *Multiphase flow in porous media: I. macroscopic observations and modelling.* Paper presented at the SPE Annual Technical Conference and Exhibition, New Orleans, Louisiana, USA. doi: https://doi.org/10.2118/11017-MS

Sari, M., & Gürarslan, G. (2009). A sixth-order compact finite difference scheme to the numerical solutions of burgers' equation. *Applied Mathematics and Computation*, *208*(2), 475–483. doi: https://doi.org/10.1016/j.amc.2008.12.012

Shahraeeni, E., Moortgat, J., & Firoozabadi, A. (2015). High-resolution finite element methods for 3d simulation of compositionally triggered instabilities in porous media. *Computers & Geosciences*, *19*, 899–920. doi: https://doi.org/10.1007/s10596-015-9501-z

Sharma, V., Nand, S., Pramanik, S., Chen, C.-Y., & Mishra, M. (2020). Control of radial miscible viscous fingering. *Journal of Fluid Mechanics*, *884*, A16. doi: https://doi.org/10.1017/jfm.2019.932

Shin, S., Um, E., Sabass, B., Ault, J. T., Rahimi, M., Warren, P. B., & Stone, H. A. (2016). Size-dependent control of colloid transport via solute gradients in dead-end channels. *Proceedings of the National Academy of Sciences*, *113*(2), 257–261. doi: https://doi.org/10.1073/pnas.1511484112

Szymczak, P., & Ladd, A. J. C. (2009). Wormhole formation in dissolving fractures. *Journal of Geophysical Research: Solid Earth*, *114*(B6), 1277–1340. doi: https://doi.org/10.1029/2008JB006122

Tan, C. T., & Homsy, G. M. (1988). Simulation of nonlinear viscous fingering in miscible displacement. *The Physics of Fluids*, *31*(6), 1330-1338. doi: https://doi.org/10.1063/1.866726

Tchelepi, H. A., & Orr, F. M. (1994). Interaction of viscous fingering, permeability heterogeneity, and gravity segregation in three dimensions. *SPE Reservoir Engineering*, *9*(4), 266–271. doi: https://doi.org/10.2118/25235-PA

Turner, G. A. (1959). The frequency response of some illustrative models of porous media: Experiments and computations with two artificial packed beds to illustrate a method of determining parameters of the bed. *Chemical Engineering Science*, *10*(1), 14–21. doi: https://doi.org/10.1016/0009-2509(59)80020-8

van Genuchten, M. T., & Wierenga, P. J. (1976). Mass transfer studies in sorbing porous media, 1, analytical solutions. *Soil Science Society of America Journal*, *40*, 473–480. doi: https://doi.org/10.2118/14898-PA

Vasilyeva, M., Babaei, C. E. T., M., & Alekseev, V. (2006). Upscaling of the single-phase flow and heat transport in fractured geothermal reservoirs using nonlocal multicontinuum method. *Computational Geosciences*, *23*, 745–759. doi: https://doi.org/10.1007/s10596-019-9817-1

Wever, D. A. Z., Picchioni, F., & Broekhuis, A. A. (2013). Comblike polyacrylamides as flooding agent in enhanced oil recovery. *Industrial & Engineering Chemistry Research*, *52*(46), 16352–16363. doi: https://doi.org/10.1021/ie402526k

Yuan, Q., & Azaiez, J. (2014). Miscible displacements in porous media with time-dependent injection velocities. *Transport in Porous Media*, *104*, 57—76. doi: https://doi.org/10.1007/s11242-014-0320-9

Yuan, Q., & Azaiez, J. (2015). Inertial effects of miscible viscous fingering in a hele-shaw cell. *Fluid Dynamics Research*, *47*, 015506. doi: https://doi.org/10.1088/0169-5983/47/1/015506

Yuan, Q., Yao, S., Zhou, X., Zeng, F., Knorr, K. D., & Imran, M. (2017a). Miscible displacements with concentration-dependent diffusion and velocity-induced dispersion in porous media. *Journal of Petroleum Science and Engineering*, *159*, 344–359. doi: https://doi.org/10.1016/j.petrol.2017.09.030

Yuan, Q., Zhou, X., Zeng, F., Knorr, K. D., & Imran, M. (2017b). Nonlinear simulation of miscible displacements with concentration-dependent diffusion coefficient in homogeneous porous media. *Chemical Engineering Science*, *172*, 528–544. doi: https://doi.org/10.1016/j.ces.2017.07.009

Zhao, C., Hobbs, B. E., Regenauer-Lieb, K., & Ord, A. (2011). Computational simulation for the morphological evolution of nonaqueous phase liquid dissolution fronts in two-dimensional fluid-saturated porous media. *Computers & Geosciences*, *15*, 167–183. doi: https://doi.org/10.1007/s10596-010-9206-2

Zimmerman, W. B., & Homsy, G. M. (1991). Nonlinear viscous fingering in miscible displacement with anisotropic dispersion. *Physics of Fluids A: Fluid Dynamics*, *3*(8), 1859–1872. doi: https://doi.org/10.1063/1.857916